



X-ray diffraction and Raman spectra of merrillite at high pressures

Muhua Jia , Xin Hu , Yungui Liu , Sheng Jiang , Xiang Wu & Shuangmeng Zhai

To cite this article: Muhua Jia , Xin Hu , Yungui Liu , Sheng Jiang , Xiang Wu & Shuangmeng Zhai (2020) X-ray diffraction and Raman spectra of merrillite at high pressures, High Pressure Research, 40:3, 411-422, DOI: [10.1080/08957959.2020.1798945](https://doi.org/10.1080/08957959.2020.1798945)

To link to this article: <https://doi.org/10.1080/08957959.2020.1798945>



Published online: 29 Jul 2020.



Submit your article to this journal [↗](#)



Article views: 30



View related articles [↗](#)



View Crossmark data [↗](#)



X-ray diffraction and Raman spectra of merrillite at high pressures

Muhua Jia^{a,b}, Xin Hu^{a,b}, Yungui Liu^c, Sheng Jiang^{ib}^d, Xiang Wu^c and Shuangmeng Zhai^a

^aKey Laboratory of High-Temperature and High-Pressure Study of the Earth's Interior, Institute of Geochemistry, Chinese Academy of Sciences, Guiyang, People's Republic of China; ^bUniversity of Chinese Academy of Sciences, Beijing, People's Republic of China; ^cState Key Laboratory of Geological Processes and Mineral Resources, China University of Geosciences, Wuhan, People's Republic of China; ^dShanghai Synchrotron Radiation Facility (SSRF), Shanghai Advanced Research Institute, Chinese Academy of Sciences, Shanghai, People's Republic of China

ABSTRACT

The compressibility and effect of pressure on the vibrations of merrillite, $\text{Ca}_9\text{NaMg}(\text{PO}_4)_7$, were studied by using diamond anvil cell at room temperature combined with *in-situ* synchrotron X-ray diffraction and Raman spectroscopy up to about 18 and 15 GPa, respectively. The pressure-volume data was fitted by a third-order Birch–Murnaghan equation of state to determine the isothermal bulk modulus as $K_0 = 87.2(32)$ GPa with pressure derivative $K_0' = 3.2(4)$. If $K_0' = 4$, the isothermal bulk modulus was obtained as 81.6 (10) GPa. The axial compressibility was estimated and an axial elastic anisotropy exists since *a*-axis is less compressible than the *c*-axis. The Raman frequencies of all observed modes for merrillite continuously increase with pressure, and the pressure dependences of stretching modes (ν_3 and ν_1) are larger than those of the bending modes (ν_4 and ν_2) and external modes. The isothermal mode Grüneisen parameters and intrinsic anharmonicity of merrillite were also calculated.

ARTICLE HISTORY



Received 30 December 2019
Accepted 17 July 2020

KEYWORDS

Merrillite; $\text{Ca}_9\text{NaMg}(\text{PO}_4)_7$; high pressure; X-ray diffraction; Raman spectroscopy

1. Introduction

Merrillite ($\text{Ca}_9\text{NaMg}(\text{PO}_4)_7$) is an anhydrous calcium phosphate mineral found in different types of meteorites as well as lunar and Martian rocks [1–6]. Merrillite becomes increasingly attractive in studies of Mars because it is a dominant form of phosphate minerals in Martian meteorites [7], and it was thought to react in late-stage of Martian magmas [8–12]. It is also a major reservoir for rare earth elements [13–15]. Therefore, merrillite has great potential as a unique recorder of planetary magmatic compositions and conditions [16]. The physical and chemical properties of merrillite are vital to understand the differences in petrogenesis, surface processes and other thermodynamic processes among Earth, Mars, and other planetary bodies [17].

CONTACT Shuangmeng Zhai  zhaishuangmeng@mail.gyig.ac.cn  Key Laboratory of High-Temperature and High-Pressure Study of the Earth's Interior, Institute of Geochemistry, Chinese Academy of Sciences, Guiyang, Guizhou 550081, People's Republic of China

The crystal structure of merrillite is trigonal with the space group $R3c$, in which the main feature is bracelet-and-pinwheel structural unit [18–20]. The pinwheels are centered on the Mg containing an octahedron decorated by a P-centered tetrahedron with a formula of $[\text{Mg}(\text{PO}_4)_6]^{16-}$, which are connected by the interstitial complex formed of $[\text{Ca}_9\text{Na}(\text{PO}_4)]^{16+}$ units [21].

In our previous study, the thermal expansion and the effects of temperature on the vibrational modes of merrillite at high-temperature have been investigated [22]. However, there is no report about the physical and chemical properties of merrillite under high pressures. In this study, the high pressure behaviors of merrillite were investigated through *in-situ* X-ray diffraction and Raman spectroscopic measurements at room temperature. The compressibility of merrillite was determined. The effect of pressure on the lattice parameters and the characteristics of Raman active modes of merrillite is quantitatively analyzed. In addition, the isothermal mode Grüneisen parameters were calculated. Combined with the previous results, the intrinsic anharmonic parameters were obtained as non-zero, indicating an intrinsic anharmonicity.

2. Experimental

High-purity merrillite was synthesized by solid-state reactions methods, which is described in our previous study [22]. The starting material was mixed from reagent-grade $\text{NH}_4\text{H}_2\text{PO}_4$, CaCO_3 , Na_2CO_3 and MgO powders in the proportion of the stoichiometric $\text{Ca}_9\text{NaMg}(\text{PO}_4)_7$. Prior to synthesizing the merrillite, reagent graded CaCO_3 , Na_2CO_3 and MgO powders were dried overnight in a vacuum oven at 473 K. Then the reagents were quickly weighted and the mixture was grounded sufficiently and heated at 1373 K for 48 h. The final product was examined by powder X-ray diffractometer as a single phase of $\text{Ca}_9\text{NaMg}(\text{PO}_4)_7$ merrillite.

The high pressure X-ray diffraction experiments were carried out using symmetric piston cylinder with a diamond anvil cell (DAC) with 300- μm culets. The rhenium gasket was pre-intended to a thickness of 45 μm with a hole of 180 μm in diameter and was used as the sample chamber. A small piece of sample was loaded into the chamber. Silicone oil was loaded as pressure-transmitting medium and a small piece of gold was used as the pressure calibrant [23]. The *in-situ* angle dispersive synchrotron X-ray diffraction patterns at various pressures were collected at the beamline BL15U1 of Shanghai Synchrotron Radiation Facility (SSRF) [24]. A monochromatic X-ray beam with the wavelength of 0.6199 Å and a beam size of 2 μm (width) \times 3 μm (height) were used. The sample-to-detector distance and the geometrical parameters of the detector were calibrated with cerium dioxide (CeO_2). Two-dimensional images were collected by a MAR-165 charge-couple device (CCD) detector and integrated using the Dioptas program to one-dimensioned diffraction patterns [25]. All obtained X-ray diffraction patterns were analyzed by the GSAS software package [26] to determine the lattice parameters.

The high pressure Raman spectra were collected by a symmetric piston cylinder DAC with 400- μm culets (type-Ia). A hole of 240 μm in diameter drilled at the pre-intended T301 stainless steel gasket (in a thickness of ~ 70 μm) was used as the sample chamber. Argon was loaded as pressure-transmitting medium. A small piece of sample was loaded into the sample chamber with a ruby sphere as the pressure marker. The pressure was determined according to the ruby fluorescence method [27]. The Raman spectra of synthetic merrillite at various pressures and room temperature were collected by Horiba

LabRam HR Evolution micro-Raman spectrometer with a 1800 lines/mm grating. The procedures are similar to the previous study [22]. A YAG: Nd³⁺ laser with a wavelength of 532 nm was used as an exciting source. An SLM Plan 50× Olympus microscope objective was used to focus the laser beam and collect the scattered light. The accumulation time of each spectrum was 60 s. Each Raman spectrum was analyzed by using the PeakFit program (SPSS Inc., Chicago).

3. Results and discussion

3.1. High pressure *in-situ* X-ray diffraction

The high pressure *in-situ* X-ray diffraction patterns of merrillite were recorded up to 18.08 GPa, and no pressure-induced phase transition was observed. The typical *in-situ* X-ray diffraction patterns of merrillite at different pressures and room temperature are shown in Figure 1. With increasing pressure, the X-ray diffraction peaks shift to higher 2θ region. The powder X-ray diffraction data of merrillite at ambient conditions after high pressure experiments yielded unit-cell parameters of $a_0 = 10.340(1)$ Å, $c_0 = 37.027(7)$ Å, and $V_0 = 3428.2(6)$ Å³, which are consistent with a previous study of Morozov et al. [28] (*i.e.* $a_0 = 10.3397$ Å, $c_0 = 37.0290$ Å, $V_0 = 3428.38$ Å³).

A GSAS refined plot of X-ray diffraction pattern collected at a pressure of 2.80 GPa is shown in Figure 2. The refined unit-cell parameters of merrillite at different pressures are listed in Table 1. The P - V data has been fitted to the third-order Birch–Murnaghan

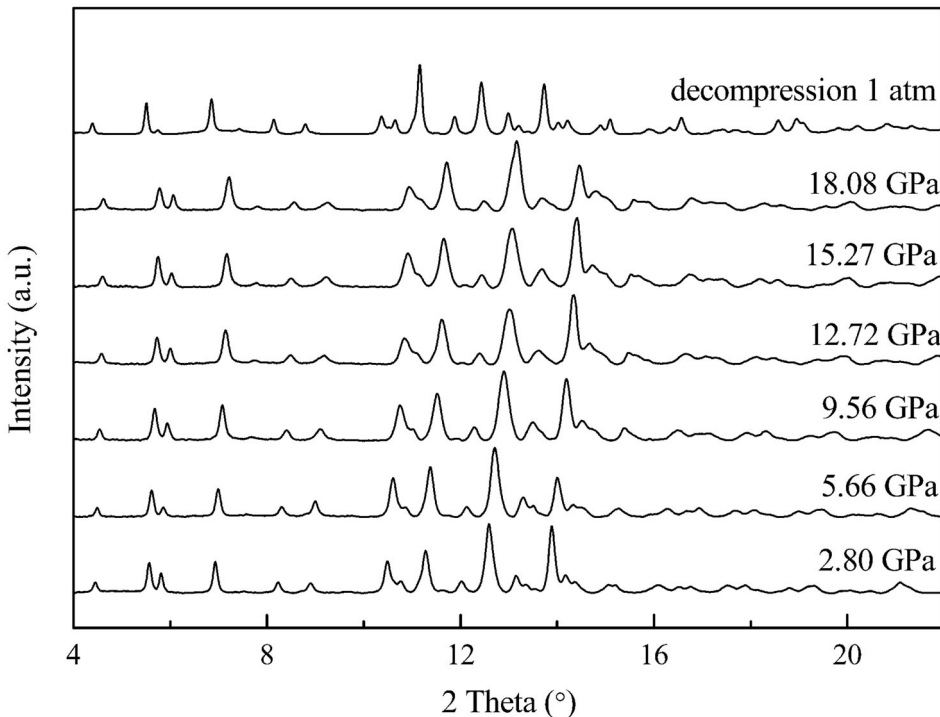


Figure 1. Representative X-ray diffraction patterns of merrillite up to 18.08 GPa at room temperature.

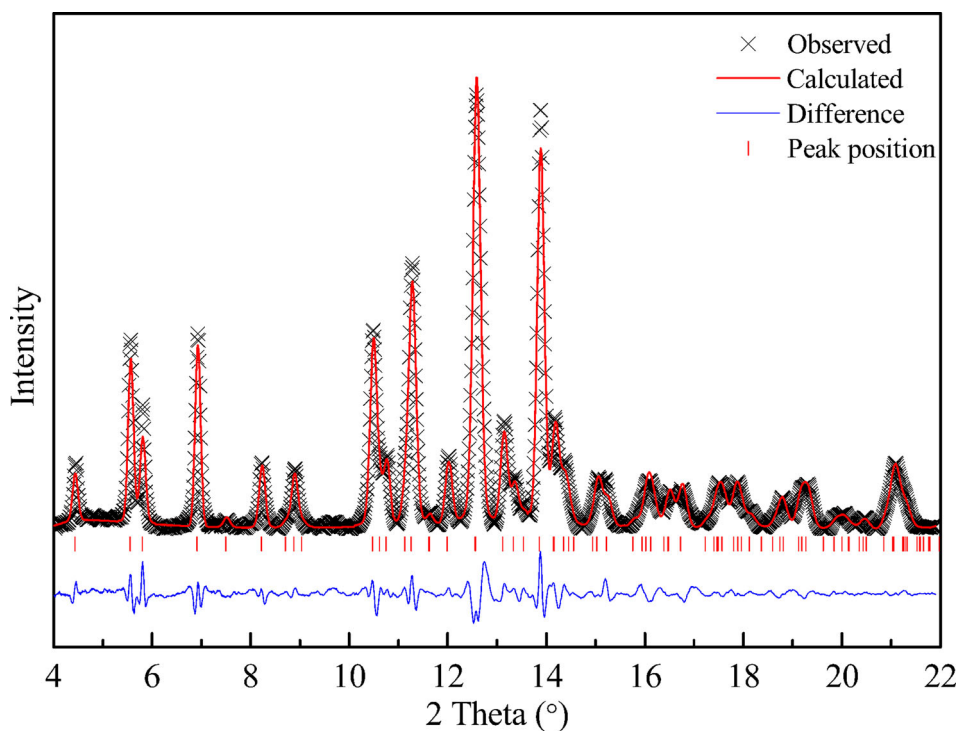


Figure 2. Refined X-ray diffraction pattern of merrillite obtained at 2.80 GPa. Observed spectra (black crosses), calculated spectra (line) and difference plot (bottom curve) and peak position are shown.

Table 1. Unit-cell parameters and volume of merrillite at different pressures.

P (GPa)	a (Å)	c (Å)	V (Å ³)
0.00(1)	10.340(1)	37.027(7)	3428.2(6)
1.12(1)	10.306(1)	36.902(4)	3394.6(5)
2.80(1)	10.257(1)	36.665(5)	3340.5(6)
4.02(1)	10.224(1)	36.513(4)	3294.1(5)
4.49(1)	10.198(1)	36.461(6)	3282.6(5)
4.92(1)	10.189(1)	36.406(7)	3271.8(6)
5.66(1)	10.167(1)	36.268(5)	3242.9(8)
7.63(1)	10.104(1)	36.020(8)	3184.8(8)
8.54(1)	10.076(1)	35.897(8)	3156.5(8)
9.04(1)	10.048(1)	35.822(10)	3132.2(9)
9.56(1)	10.044(1)	35.773(8)	3125.4(8)
10.40(1)	10.010(1)	35.681(6)	3096.0(8)
10.76(1)	9.996(1)	35.673(9)	3086.6(9)
11.18(1)	9.989(1)	35.635(4)	3079.4(5)
11.74(1)	9.982(1)	35.544(5)	3067.1(4)
12.72(1)	9.963(1)	35.498(6)	3051.4(7)
14.90(2)	9.899(1)	35.262(7)	2992.1(7)
15.27(2)	9.897(1)	35.258(5)	2991.0(5)
16.83(2)	9.862(1)	35.135(7)	2959.1(8)
17.07(2)	9.859(1)	35.097(6)	2954.6(7)
18.08(2)	9.837(1)	34.982(7)	2931.1(8)

Note: Values in parentheses are errors.

equation of state [29] to determine the elastic parameters:

$$P = \frac{3K_0}{2} \left[\left(\frac{V_0}{V} \right)^{\frac{7}{3}} - \left(\frac{V_0}{V} \right)^{\frac{5}{3}} \right] \left\{ 1 + \frac{3}{4} (K'_0 - 4) \left[\left(\frac{V_0}{V} \right)^{\frac{2}{3}} - 1 \right] \right\}$$

where P and V are pressure and volume, and V_0 , K_0 , K'_0 are zero-pressure volume, isothermal bulk modulus and its pressure derivation, respectively. The results from a least-squares fitting using an *EosFit* program [30] are $V_0 = 3437.3(41) \text{ \AA}^3$, $K_0 = 87.2(32) \text{ GPa}$, $K'_0 = 3.2(4)$. When fix $K'_0 = 4$, the fitting yields $K_0 = 81.6(10)$. The unit-cell volume variation of merrillite as a function of pressure and the compression curve calculated by the fitted parameters are plotted in Figure 3.

The changes of lattice parameters a and c as a function of pressure are also plotted in Figure 3. By fitting a third-order Birch–Murnaghan EoS and following the procedure implemented in the *EosFit* program, the axial compressibility of merrillite as functions of

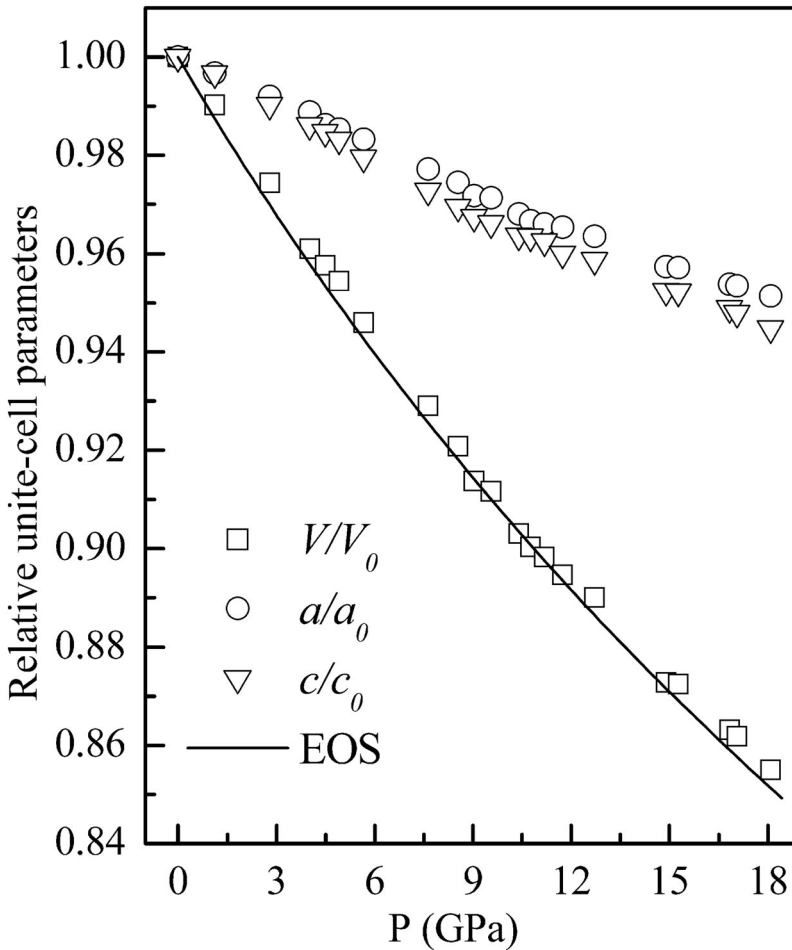


Figure 3. Relative changes in unit-cell parameters and volume with pressure.

pressure can be obtained. For comparison, the $K'_0 = 4$ was fixed. The fitting axial moduli are $Ka_0 = 85.0(15)$ GPa and $Kc_0 = 72.9(10)$ GPa. This clearly shows that merrillite has axial elastic anisotropy along the a - and c -axis. There are two possible reasons for axial elastic anisotropy. One might be attributed to the structure of merrillite. In the crystal structure, the a -parallel structural channels must traverse the fairly inert 'bracelet-and-pinwheel' structural unit that has larger atom density, whereas channels parallel to c -axis does not. So a -axis has a bit tighter arrangement than c -axis [22]. The other reason is due to the different compressibility between different polyhedron. The a -axis mainly consists of the PO_4 tetrahedron, while the c -axis is mainly composed of CaO polyhedron [19]. Because the phosphate tetrahedron are much less compressible compared to the calcium polyhedron [31], the change in the volume of PO_4 tetrahedron at high pressure is smaller than the volume of CaO polyhedron.

3.2. High pressure Raman spectra

As mentioned above, merrillite has a trigonal structure belonging to the space group $R3c$ ($C_{3v}(3m)$). According to the factor group theory [32], it gives two acoustic modes and 182 optical modes, as following:

$$\Gamma_{\text{acoustic}} = A_1 + E$$

$$\Gamma_{\text{optic}} = 45A_1(R, IR) + 46A_2 + 91E(R, IR)$$

In the optical modes, 136 Raman active modes are predicated. The Raman spectra of merrillite were collected in the pressure range from 0 to 15.3 GPa at room temperature.

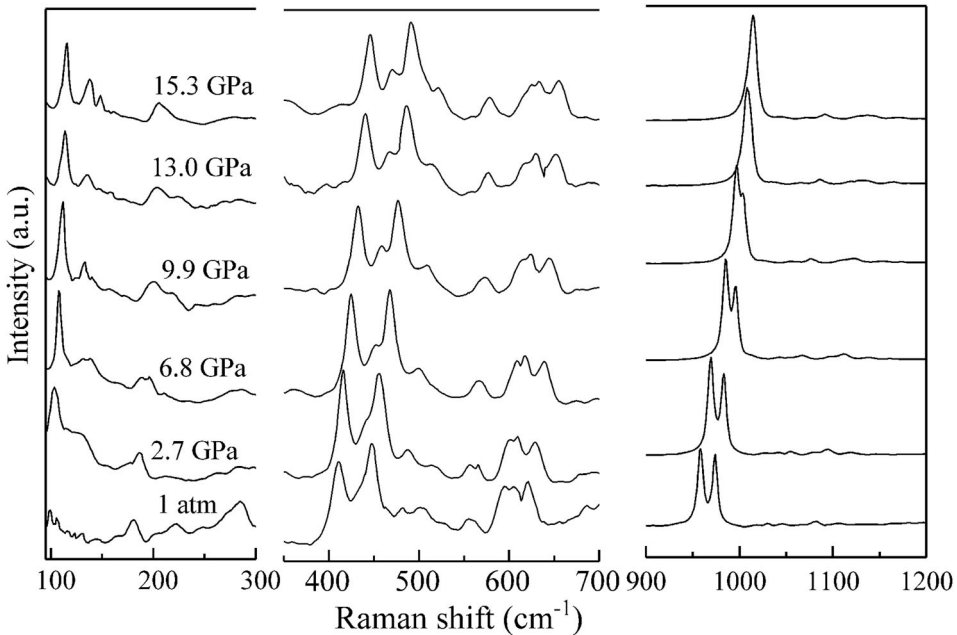


Figure 4. Typical Raman spectra of merrillite at different pressures and room temperature.

The typical Raman spectra of merrillite at different pressures are shown in [Figure 4](#). No pressure-induced phase transformation occurs. At ambient conditions, sixteen Raman peaks are distinguished. Similar to a previous study [33], the spectrum of merrillite includes an obvious strong doublet at 975 and 960 cm^{-1} associated with ν_1 symmetric stretching vibrations of the P-O bands in PO_4 tetrahedron. The weak bands at 1083 and 1029 cm^{-1} are for ν_3 anti-symmetric stretching vibrations of the P-O bands. The bands at 480, 448, 434 and 410 cm^{-1} are for ν_2 bending vibrations, and the bands at 621, 605, 594 and 554 cm^{-1} are for ν_4 bending vibrations, corresponding to the O-P-O bending vibration within the PO_4 tetrahedron. The bands below 400 cm^{-1} at 99, 180, 224, and 246 cm^{-1} are assigned to the external modes.

With increasing pressure, the peaks at 960 and 975 cm^{-1} tend to merge into one band and the splitting peak at 448 cm^{-1} becomes obvious, as shown in [Figure 4](#). It indicates that the compression-induced coalescence of these bands may be attributed to the local crystal field surrounding the PO_4 tetrahedra deviates less from tetrahedral symmetry with increasing pressure [34,35]. In the doublets mentioned above, the shift of the 960 cm^{-1} is always higher than the shift of 975 cm^{-1} with pressure. Therefore, the separations tend to decrease with pressure. The same phenomenon occurs in $\beta\text{-Ca}_3(\text{PO}_4)_2$ [35]. These changes are not due to a displacive phase transition since no new peak appears in the high pressure X-ray diffraction patterns. It may be attributed to the resonance effect.

Generally, the Raman bands of vibrational modes shift to higher frequency regions with increasing pressures. The variations of Raman frequencies with pressure for all observed modes are illustrated in [Figure 5](#). The pressure-dependent of Raman shift in $\text{Ca}_9\text{NaMg}(\text{PO}_4)_7$ shows a continuous and nearly linear blueshift with pressure, suggesting the compression-induced structural changes including the decreases of bond length in PO_4 tetrahedron and other polyhedra. It is reasonable since the chemical bonds generally become shorter with increasing pressures. According to Hooke's law, shorter bonds indicate stiffening of bands, corresponding to higher vibrational frequency. The constants derived by linear regressions of $\nu_i = \nu_{0i} + a_i P$ are listed in [Table 2](#). All observed bands show positive pressure dependences. The pressure dependences of anti-symmetric stretching and symmetric stretching modes (ν_3 and ν_1) are larger than those of the bending modes (ν_4 and ν_2) and the external modes. In fact, the pressure coefficients of ν_3 and ν_1 modes are 3.09–4.05 $\text{cm}^{-1} \text{GPa}^{-1}$, whereas the coefficients for ν_4 , ν_2 and the external modes are 0.91–2.90 $\text{cm}^{-1} \text{GPa}^{-1}$, indicating that the stretching vibrations are more sensitive to pressure than the bending vibrations and the external modes. Similar observations have been found on some other minerals, such as $\beta\text{-Mg}_2\text{SiO}_4$ [36], $\beta\text{-Ca}_3(\text{PO}_4)_2$ [35], and grossular [37]. These minerals show strong dependences of their P-O (Si-O) stretching modes with increasing pressure, while P-O-P (Si-O-Si) bending modes are only slightly affected by pressure. The reason may be attributed to the structural evolution of PO_4 or SiO_4 tetrahedron at high pressure, and more high pressure single crystal works are required.

3.3. Isothermal mode Grüneisen parameters

Based on the obtained isothermal bulk modulus and pressure-dependence of Raman vibrations, the isothermal mode Grüneisen parameters γ_{IT} can be calculated by following

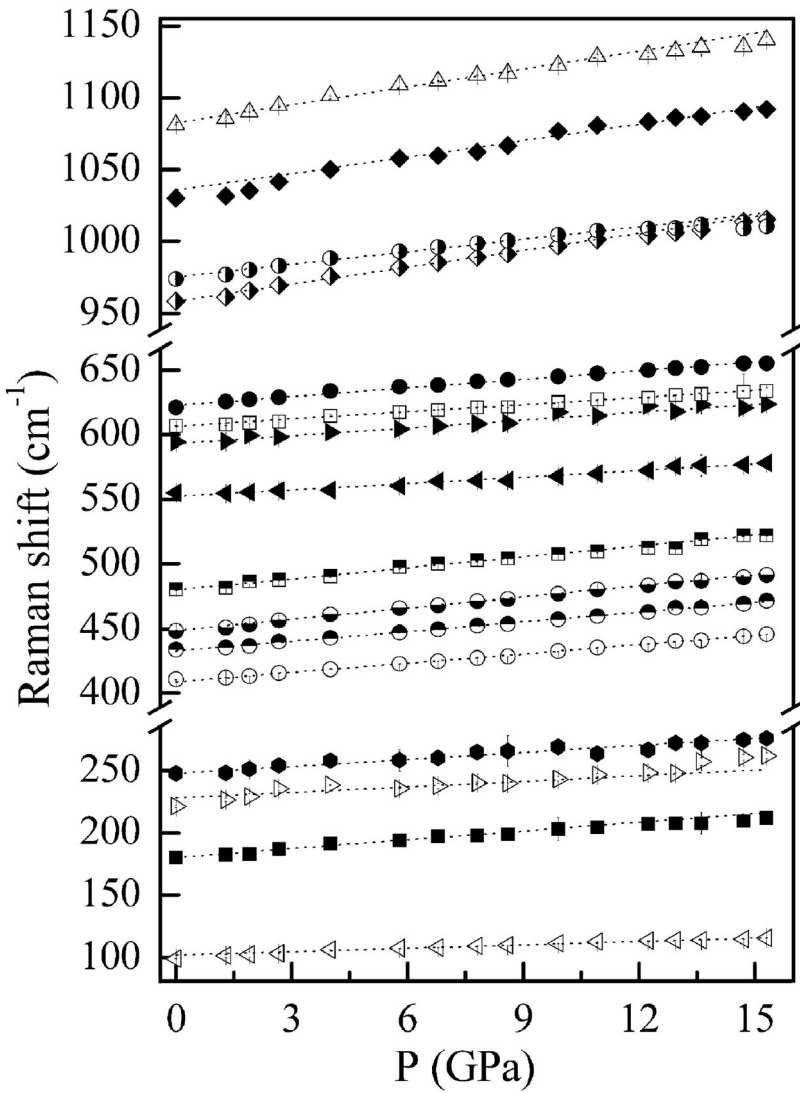


Figure 5. Pressure dependences of the Raman bands of merrillite at room temperature. The different symbols represent the different Raman active vibrations as listed in Table 2.

expression [38]:

$$\gamma_{iT} = \frac{\left(\frac{\delta \nu_i}{\delta P}\right) K_0}{\nu_i}$$

where ν_i is the vibrational frequency of the i^{th} band, and K_0 is the isothermal bulk modulus. The isothermal bulk modulus $K_0 = 87.2(32)$ GPa obtained in this study was used. The values of γ_{iT} for different modes of merrillite are also listed in Table 2.

For the internal modes PO_4 in merrillite, the average value of isothermal mode Grüneisen parameters is 0.38, which is similar to that of tuite [39] and smaller than that of

Table 2. Constants determined in $\nu_i = \nu_{0i} + a_i P$ and the values of γ_{iT} , γ_{iP} and β_i of each vibrational mode for merrillite.

	$\nu_{i,0}$	ν_{0i}	a_i	R^2	γ_{iT}	γ_{iP}	$\beta_i \times 10^{-5}$
PO ₄ modes ν_3	1083	1082.9(2)	4.05(13)	0.985	0.33	0.65	-1.56
	1029	1035.7(2)	3.83(2)	0.966	0.32	0.61	-1.41
ν_1	975	974.6(5)	3.09(9)	0.987	0.28	0.45	-0.83
	960	958.6(5)	3.90(8)	0.994	0.35	0.37	-0.10
ν_4	621	622.9(1)	2.23(1)	0.994	0.31	0.61	-1.46
	605	606.7(2)	1.85(2)	0.995	0.27	0.54	-1.31
	594	593.1(3)	2.02(3)	0.966	0.30	0.48	-0.88
	554	552.2(2)	1.67(2)	0.998	0.26	0.25	0.05
ν_2	480	480.1(2)	2.81(2)	0.986	0.51	0.92	-1.99
	448	448.5(1)	2.90(1)	0.997	0.56	0.84	-1.36
	434	432.7(3)	2.50(3)	0.998	0.58	-	-
	410	408.8(1)	2.39(1)	0.997	0.51	0.50	0.05
External mode	246	247.5(11)	1.88(9)	0.986	0.66	1.730	-5.20
	224	227.9(4)	1.48(5)	0.673	0.57	2.06	-7.24
	180	180.3(1)	2.35(2)	0.987	1.14	2.70	-7.58
	99	101.9(1)	0.91(1)	0.987	0.78	5.27	-21.82

Notes: ν_i and ν_{0i} are in cm^{-1} , P in GPa, and the constant a_i has the corresponding units. R^2 is the correlation coefficient. Mode Grüneisen parameter γ_{iT} is calculated with isothermal bulk modulus of $K_0 = 87.2$ GPa obtained in this study. γ_{iP} are from previous study.

fluorapatite [40]. It might be attributed to the structural evolution of PO₄ tetrahedron at high pressures, which is related to the crystal structure (arrangement of atoms) and compressibility. Compared with SiO₄ modes in other silicate minerals such as pyrope [37] and zircon [41], the average value of the PO₄ isothermal mode Grüneisen parameters in phosphate minerals is relatively low, which may be attributed to the SiO₄ tetrahedron which is less compressible than PO₄ tetrahedron.

The values of γ_{iT} are in the range of 0.26 ~ 0.58 for the internal PO₄ modes and 0.57 ~ 1.14 for the external modes. In fact, the average value for isothermal mode Grüneisen parameters of four external modes is 0.79 in low-frequency, about two times larger than the average value of internal PO₄ modes in high-frequency. Therefore, the evolution of PO₄ is not representative to the structural evolution of Ca₉NaMg(PO₄)₇ merrillite containing complex bracelet-and-pinwheel units. The external modes strongly affect the isothermal mode Grüneisen parameters, and such behavior is also observed in Ca₂GeO₄ [42].

3.4. Intrinsic anharmonicity

Intrinsic anharmonicity is a measure of the effect of temperature at constant volume on mode frequency and non-parabolic shape of the interatomic potential [43]. Therefore, it is an important parameter for thermodynamic properties of minerals at high pressure and temperature conditions. As shown in Table 2, the values of isothermal mode Grüneisen parameters and those of isobaric mode Grüneisen parameters for the same vibrations are not equal. Therefore, an intrinsic anharmonicity exists. The intrinsic anharmonic mode parameter β_i can be estimated using the values of thermal expansion coefficient α (reported as $4.86 \times 10^{-5} \text{ K}^{-1}$ [22]), Grüneisen parameters γ_{iP} and γ_{iT} as follows [44]:

$$\beta_i = \left(\frac{\partial \ln \nu_i}{\partial T} \right)_v = \alpha (\gamma_{iT} - \gamma_{iP}) T$$

The values of calculated β_i for different vibrational modes are shown in Table 2, ranging from $-21.82 \times 10^{-5} \text{ K}^{-1}$ to $0.05 \times 10^{-5} \text{ K}^{-1}$ with an average intrinsic anharmonic mode parameter for PO_4 of $-0.98 \times 10^{-5} \text{ K}^{-1}$. The absolute intrinsic anharmonic mode parameters of merrillite is higher than those of tuite ($-0.80 \times 10^{-5} \text{ K}^{-1}$) [39] and fluorapatite ($0.55 \times 10^{-5} \text{ K}^{-1}$) [40]. Compared with SiO_4 vibrations in silicate minerals such as grossular ($-1.75 \times 10^{-5} \text{ K}^{-1}$) [37], the PO_4 vibrations in merrillite show lower absolute intrinsic anharmonic mode parameters.

4. Conclusions

The elasticity and effects of pressure on the vibrational modes of merrillite have been investigated by using synchrotron *in-situ* X-ray diffraction and Raman spectroscopic measurements. No phase transition occurs in the present study. The isothermal bulk modulus was obtained as $K_0 = 87.2(32) \text{ GPa}$ with $K'_0 = 3.2(4)$. An axial elastic anisotropy exists along the *a*- and *c*-axis. The Raman frequencies of all observed PO_4 modes for merrillite continuously increase with pressure, and the pressure dependences of anti-symmetric stretching and symmetric stretching modes (ν_3 and ν_1) are larger than those of the bending modes (ν_4 and ν_2) and the external modes. The isothermal mode Grüneisen parameters and intrinsic anharmonic parameters of merrillite were calculated by using present results, and an average isobaric Grüneisen parameter and intrinsic anharmonic parameters of the internal PO_4 modes was obtained as 0.38 and $-0.98 \times 10^{-5} \text{ K}^{-1}$, respectively.

Acknowledgements

The *in-situ* X-ray diffraction measurements were carried out with the help from members of BL15U1, SSRF, China (Proposal No. 2018-SSRF-PT-007075).

Disclosure statement

No potential conflict of interest was reported by the author(s).

Funding

This work was financially supported by the Strategic Priority Research Program of Chinese Academy of Sciences (grant number XDB41000000), the Science and Technology Department of Guizhou Province (grant number [2016] 1157).

ORCID

Sheng Jiang  <http://orcid.org/0000-0002-2570-6654>

References

- [1] Terada K, Monde T, Sano Y. Ion microprobe U-Th-Pb dating of phosphates in Martian meteorite ALH 84001. *Meteorit Planet Sci.* 2003;38:1697–1703. doi:10.1111/j.1945-5100.2003.tb00009.x.

- [2] Mcsween HY, Eisenhour DD, Taylor LA, et al. QUE94201 shergottite: crystallization of a Martian basaltic magma. *Geochim Cosmochim Acta*. 1996;60:4563–4569. doi:10.1016/S0016-7037(96)00265-7.
- [3] Adcock CT, Hausrath EM, Forster PM, et al. Synthesis and characterization of the Mars-relevant phosphate minerals Fe- and Mg-whitlockite and merrillite and a possible mechanism that maintains charge balance during whitlockite to merrillite transformation. *Am Mineral*. 2014;99:1221–1232. doi:10.2138/am.2014.4688.
- [4] Jolliff BL, Haskin LA, Colson RO, et al. Partitioning in REE-saturating minerals: theory, experiment, and modelling of whitlockite, apatite, and evolution of lunar residual magmas. *Geochim Cosmochim Acta*. 1993;57:4069–4094. doi:10.1016/0016-7037(93)90354-Y.
- [5] Llorca J, Trigo-Rodríguez JM. Raman spectroscopy of merrillite in Villalbeto de la Peña L6 ordinary chondrite. 37th Lunar Planet Sci Conf. 2006;34:1055–1056.
- [6] Shearer CK, Papike JJ, Burger PV, et al. Direct determination of europium valence state by XANES in extraterrestrial merrillite: implications for REE crystal chemistry and Martian magmatism. *Am Mineral*. 2011;96:1418–1421. doi:10.2138/am.2011.3860.
- [7] McSween H, Treiman AH. Martian meteorites. In: J Papike, editor. *Planetary Materials*. Chantilly, VA: Reviews in Mineralogy, Mineralogical Society of America; 1998. 36: p. F1–F53.
- [8] McCubbin FM, Shearer CK, Burger PV, et al. Volatile abundances of coexisting merrillite and apatite in the martian meteorite Shergotty: implications for merrillite in hydrous magmas. *Am Mineral*. 2014;99:1347–1354. doi:10.2138/am.2014.4782.
- [9] Douce AEP, Roden MF, Chaumba J, et al. Compositional variability of terrestrial mantle apatites, thermodynamic modeling of apatite volatile contents, and the halogen and water budgets of planetary mantles. *Chem Geol*. 2011;288:14–31. doi:10.1016/j.chemgeo.2011.05.018.
- [10] Filiberto J, Treiman AH. Martian magmas contained abundant chlorine, but little water. *Geology*. 2009;37:1087–1090. doi:10.1130/G30488A.1.
- [11] Mysen BO, Virgo D, Popp RK, et al. The role of H₂O in Martian magmatic systems. *Am Mineral*. 1998;83:942–946. doi:10.2138/am-1998-9-1002.
- [12] Gross J, Filiberto J, Herd CDK, et al. Petrography, mineral chemistry, and crystallization history of olivine-phyric shergottite NWA 6234: a new melt composition. *Meteorit Planet Sci*. 2013;48:854–871. doi:10.1111/maps.12092.
- [13] Crozaz G, Zinner E, Delaney JS. Rare earth element concentrations of mesosiderite merrillite. *Meteorit*. 1985;20:629–630. doi:10.1007/BF01646385.
- [14] Reed SJB, Smith DGW. Ion probe determination of rare earth elements in merrillite and apatite in chondrites. *Earth Planet Sci Lett*. 1985;72:238–244. doi:10.1016/0012-821X(85)90008-1.
- [15] Jolliff BL, Freeman JJ, Wopenka B. Structural comparison of lunar, terrestrial, and synthetic whitlockite using laser Raman microprobe spectroscopy. *Lunar Planet Sci*. 1996;27:613–614.
- [16] Jolliff BL. Merrillite and apatite as recorders of planetary magmatic processes. *Am Mineral*. 2014;99:2161–2162. doi:10.2138/am-2014-5075.
- [17] Adcock CT, Hausrath EM, Forster PM. Readily available phosphate from minerals in early aqueous environments on Mars. *Nat Geosci*. 2013;6:824–827. doi:10.1038/ngeo1923.
- [18] Xie X, Yang H, Gu X, et al. Chemical composition and crystal structure of merrillite from the Suizhou meteorite. *Am Mineral*. 2015;100:2753–2756. doi:10.2138/am-2015-5488.
- [19] Hughes JM, Jolliff BL, Gunter ME. The atomic arrangement of merrillite from the Fra Mauro Formation, Apollo 14 lunar mission: the first structure of merrillite from the Moon. *Am Mineral*. 2006;91:1547–1552. doi:10.2138/am.2006.2021.
- [20] Moore PB. Bracelets and pinwheels: a topological-geometrical approach to the calcium orthosilicate and alkali sulfate structures. *Am Mineral*. 1973;58:32–42.
- [21] Hawthorne FC. Graphical enumeration of polyhedral clusters. *Acta Crystallogr*. 1983;A39:724–736. doi:10.1107/S0108767383001452.
- [22] Jia M, Zhai K, Gao M, et al. Raman spectra and X-ray diffraction of merrillite at various temperatures. *Vib Spectrosc*. 2020;106:103005, doi:10.1016/j.vibspec.2019.103005.
- [23] Fei Y, Ricolleau A, Frank M, et al. Toward an internally consistent pressure scale. *Proc Natl Acad Sci*. 2007;104:9182–9186. doi:10.1073/pnas.0609013104.

- [24] Zhang L, Yan S, Jiang S, et al. Hard X-ray micro-focusing beamline at SSRF. *Nucl Sci Tech*. 2015;26:060101–060107. doi:10.13538/j.1001-8042/nst.26.060101.
- [25] Hammersley AP, Svensson SO, Hanfland M, et al. Two-dimensional detector software: from real detector to idealised image or two-theta scan. *High Press Res*. 1996;14:235–248. doi:10.1080/08957959608201408.
- [26] Larson AC, Von Dreele RB. General structure analysis system GSAS. Los Alamos National Laboratory Report LAUR. 1994: 86–748.
- [27] Mao HK, Xu J, Bell PM. Calibration of the ruby pressure gauge to 800 kbar under quasi-hydrostatic conditions. *J Geophys Res: Solid Earth*. 1986;91:4673–4676. doi:10.1029/JB091iB05p04673.
- [28] Morozov VA, Presniakov IA, Belik AA, et al. Crystal structures of calcium magnesium alkali metal phosphates $\text{Ca}_9\text{MgM}(\text{PO}_4)_7$ (M = Li, Na, K). *Kristallogra*. 1997;42:825–836. doi:10.1107/S0907444997099174.
- [29] Birch F. Finite elastic strain of cubic crystals. *Phys Rev*. 1947;71:809–824. doi:10.1103/PhysRev.71.809.
- [30] Angel RJ. Equations of state. *Rev Miner Geochem*. 2000;41:35–59. doi:10.2138/rmg.2000.41.2.
- [31] Comodi P, Liu Y, Frezzotti ML. Structural and vibrational behaviour of fluorapatite with pressure. Part I: in situ single-crystal X-ray diffraction investigation. *Phys Chem Miner*. 2001;28:219–224. doi:10.1007/s002690100154.
- [32] Kroumova E, Aroyo MI, Perez-Mato JM, et al. Bilbao crystallographic server: useful databases and tools for phase-transition studies. *Phase Transit*. 2003;76:155–170. doi:10.1080/0141159031000076110.
- [33] Xie X, Minitti ME, Chen M, et al. Natural high-pressure polymorph of merrillite in the shock veins of the Suizhou meteorite. *Geochim Cosmochim Acta*. 2002;66:2439–2444. doi:10.1016/S0016-7037(02)00833-5.
- [34] Williams Q, Knittle E. Infrared and Raman spectra of $\text{Ca}_5(\text{PO}_4)_3\text{F}_2$ -fluorapatite at high pressures: compression-induced changes in phosphate site and Davydov splittings. *J Phys Chem Solids*. 1996;57:417–422. doi:10.1016/0022-3697(95)00285-3.
- [35] Zhai S, Wu X, Xue W. Pressure-dependent Raman spectra of β - $\text{Ca}_3(\text{PO}_4)_2$ whitlockite. *Phys Chem Miner*. 2015;42:303–308. doi:10.1007/s00269-014-0720-y.
- [36] Chopelas A. Thermal properties of β - Mg_2SiO_4 at mantle pressures derived from vibrational spectroscopy: implications for the mantle at 400 km depth. *J Geophys Res*. 1991;96:11817–11830. doi:10.1029/91JB00898.
- [37] Gillet P, Fiquet G, Malézieux JM. High-pressure and high-temperature Raman spectroscopy of end-member garnets: pyrope, grossular and andradite. *Eur J Mineral*. 1992;4:651–664. doi:10.1127/ejm/4/4/0651.
- [38] Grüneisen E. Theorie des festen Zustandes einatomiger Elemente. *Ann Phys*. 1912;344:257–306. doi:10.1002/andp.19123441202.
- [39] Zhai S, Xue W, Lin CC, et al. Raman spectra and X-ray diffraction of tuite at various temperatures. *Phys Chem Miner*. 2011;38:639–646. doi:10.1007/s00269-011-0436-1.
- [40] Xue W, Zhai K, Lin CC, et al. Effect of temperature on the Raman spectra of $\text{Ca}_5(\text{PO}_4)_3\text{F}$ fluorapatite. *Eur J Mineral*. 2018;30:951–956. doi:10.1127/ejm/2018/0030-2769.
- [41] Knittle E, Williams Q. High-pressure Raman spectroscopy of ZrSiO_4 : observation of the zircon to scheelite transition at 300 K. *Am Mineral*. 1993;78:245–252.
- [42] Gillet P, Guyot F, Malezieux JM. High-pressure, high-temperature Raman spectroscopy of Ca_2GeO_4 (olivine form): some insights on anharmonicity. *Phys Earth Planet Inter*. 1989;58(2-3):141–154. doi:10.1016/0031-9201(89)90050-2.
- [43] Gillet P, Le Cléach A, Madon M. High-temperature Raman spectroscopy of SiO_2 and GeO_2 polymorphs: anharmonicity and thermodynamic properties at high-temperatures. *J Geophys Res*. 1990;95:21635–21655. doi:10.1029/JB095iB13p21635.
- [44] Mammone JF, Sharma SK. Pressure and temperature dependence of the Raman spectra of rutile-structure oxides. *Carnegie Inst. Washington, Year Book*. 1979; 369–373.